Systematic Structure-Property Relationship Studies in Palladium-Catalyzed Methane Complete Combustion

Joshua J. Willis†, Alessandro Gallo†,‡, Dimosthenis Sokaras‡, Hassan Aljama†, Stanislaw H. Nowak‡, Emmett D. Goodman†, Liheng Wu†,‡, Christopher J. Tassone‡, Thomas F. Jaramillo†, Frank Abild-Pedersen†, Matteo Cargnello*,†

†Department of Chemical Engineering and SUNCAT Center for Interface Science and Catalysis, Stanford University, Stanford, CA 94305, USA.

‡Stanford Synchrotron Radiation Lightsource, SLAC National Accelerator Laboratory, Menlo Park, CA 94025, USA.

ABSTRACT: To limit further rising levels in methane emissions from stationary and mobile sources and to enable promising technologies based on methane, development of efficient combustion catalysts that completely oxidize CH_4 to CO_2 and H_2O at low temperatures in the presence of high steam concentrations is required. Palladium is widely considered as one of the most promising materials for this reaction, and a better understanding of the factors affecting its activity and stability is crucial to design even more improved catalysts that efficiently utilize this precious metal. Here we report a study of the effect of three important variables (particle size, support, and reaction conditions including water) on the activity of supported Pd catalysts. We use uniform palladium nanocrystals as catalyst precursors to prepare a library of well-defined catalysts to systematically describe structure-property relationships with the help from theory and *in-situ* X-ray absorption spectroscopy. With this approach, we confirm that PdO is the most active phase, and that small differences in reaction rates as a function of size are likely due to variations in the surface crystal structure. We further demonstrate that the support exerts a limited influence on the PdO activity, with inert (SiO_2), acidic (Al_2O_3), and redox-active ($Ce_{0.8}Zr_{0.2}O_2$) supports providing similar rates, while basic (MgO) supports shows remarkably lower activity. Finally, we show that introduction of steam leads to a considerable decrease in rates that is due to coverage effects, rather than structural and/or phase changes. Altogether, the data suggest that to further increase activity and stability of Pd-based catalysts for methane combustion, increasing the surface area of supported PdO phases while avoiding strong adsorption of water on the catalytic surfaces is required. This study clarifies contrasting reports in the literature about active phase and stability of Pd-based materials for methane combustion.

KEYWORDS: *nanocrystals, methane complete combustion, palladium catalysts, in-situ XAS, structure-property relationships*

1. INTRODUCTION

Important advances in the extraction of natural gas from shale have allowed the U.S. to become the world's leading natural gas producer and to achieve a new record of >300 trillion cubic feet in gas reserves. The increased availability of cheap natural gas has led to renewed interest in the use of methane, its main constituent, to develop more efficient engines for transportation,[1] lower-temperature fuel cells for the effective generation of electrical energy,[2,3] and catalysts for the production of olefins and aromatics directly from methane.[4,5] In all these applications, methane combustion at low temperatures is crucial for the technologies to perform while limiting harmful methane emissions.[6] The main problems with methane utilization are its high greenhouse gas potential, much higher than CO_2[7] and the stability of the molecule that makes it rather unreactive. For these problems to be solved, methods must be developed for the activation of methane at low temperatures (<300 °C) with stable catalysts. In recent years, there have been important advances, but supported heterogeneous catalysts still require rates to be improved especially in the presence of steam.[8–16] Also, homogeneous combustion systems are far from practical due to the production of toxic gas, such as CO and NO_x.[17,18] The challenges posed by methane combustion lie in activating the strong C-H bonds in methane, while also coupling this step with activation of oxygen in sites being preferably different from those that activate the C-H bond, yet in close proximity.[11] The discovery of materials that could deliver high rates at temperatures of ~300 °C or less under demanding conditions and in the presence of poisoning species would represent a breakthrough. Palladium (Pd) is widely accepted as one of the most active methane combustion catalyst and has received continuous attention for the past few decades.[13,14,19–21] While studies in the high-temperature regime (>600 °C) have studied the kinetics and interconversion of PdO and Pd phases, there are still debated questions in the low-temperature regime.[16,22,23] Specifically, there is no consensus on the reaction active site, but strong indications have recently emerged in the literature. One challenge in identifying the active site is that the reaction is highly dependent on the Pd oxidation state, which is known to vary from metallic Pd to an intermediate chemisorbed oxygen state to bulk PdO depending upon reaction conditions (and in particular, on the oxygen chemical potential).[21] While it is generally accepted that PdO phase is the most active phase for methane combustion,[14,21,24,25] there are still questions regarding the structure of the active site, the role of the support, and the effect of steam on the structural properties of supported Pd catalysts. A systematic study of these variables is needed to precisely understand the location and nature of active sites, and in order to guide future studies to prepare more active and stable catalysts for low-temperature (<300 °C) methane combustion.

The effect of Pd particle size is of particular interest, because a change in this parameter produces materials with different exposed facets and fractions of under coordinated sites that could result in structure-sensitivity for the reaction of interest.[26] The results of studies of the effect of Pd size on activity are contrasting: some conclude that methane combustion on Pd catalysts is insensitive to particle size,[14,15,20,27] while others state that the reaction is structure-sensitive due to differences in the bond energy between palladium and oxygen at varying particle size.[13,21,28] The situation is certainly complicated by the limited control in Pd particle size in conventional materials, or by the fact that these catalysts are made using different Pd precursors, and they can be potentially contaminated from the precursor salts (e.g. chloride ions). Conclusions from studies on model single crystal surfaces also disagree in which a study of multiple palladium oxide facets showed similar activities,[15] but others suggest that the coordinatively unsaturated Pd cations on the PdO(101) facets are crucial for methane dissociation and thus combustion.[29,30] Improved synthetic techniques for supported size-controlled palladium particles would help to further our understanding of the structure-sensitivity in Pd-catalyzed methane combustion.

The support is also known to be crucial for the activity and stability of Pd catalysts. Numerous supports have been utilized for Pd-catalyzed methane combustion that can be classified as inert (e.g. silica,[31] zirconia, [13,31–33]), acid- or base- (e.g. alumina and promoted alumina,[21,27,28,31,33,34] and zeolites[35,36]), activeinthe sense that they participate in the catalytic cycle (e.g. ceria, [8,32,33,37] tin oxide, [38] and titanium oxide[32,33]). These studies have shown that the support may serve many functions, such as stabilizing the active PdO phase from thermal decomposition,[31,33,39] inhibit sintering via strong interactions with the supported PdO phase,[36] and provide reactive oxygen species during methane combustion.[40–42] It is however hard to disentangle the role of the support from other effects of Pd size and structure because supports with very different morphological properties lead to different Pd size distributions obtained by impregnations, which in turn can drastically affect its chemistry, and systematic studies of Pd-support interactions are still needed. As demonstrated in other oxidation reactions such as CO oxidation[43] and water-gas-shift reaction,[44,45] where the support can change the reaction mechanism and significantly increase reaction rates, understanding the supports' role in the mechanism for Pd–catalyzed methane combustion could help to engineer more active and stable catalysts.

An additional level of complication in the fundamental understanding of Pd-catalyzed methane combustion is represented by the presence of water (steam) during the reaction at low temperatures (<400 °C). Water is well-known to strongly deactivate Pd catalysts, even with optimized systems that show very good activity in the absence of water.[46] The effect of water depends on the temperature, and weaker effects are observed at increasing temperatures (>450 °C).[16] Kinetic experiments mostly indicate a rate order of about -1 for water indicating strong coverage of the catalytic surface during low-temperature Pd-catalyzed methane combustion.[13–16,24] A kinetic model has suggested that the strong inhibition by water is caused by its tendency to adsorb onto oxygen vacancies on the PdO surface responsible for the rate-limiting methane activation step.[13] Experimental studies have observed irreversible deactivation at low temperatures in the presence of water, suggesting that it is caused by a slow transition of the active PdO phase to an inactive $Pd(OH)_2$ surface phase.[47–49] Other studies invoke the participation of the support, with water affecting the hydroxylation of the support surface and the consequent inhibition of oxygen exchange at the metal-support interface, especially for redox-active supports.[50] For a more complete understanding of the water poisoning effect, systematic studies of the structure/size dependence, as well as support effects, on water poisoning at low temperatures would be beneficial.

We herein report a systematic study of the effects of size, support, and water inhibition on the low-temperature activity of Pd-catalyzed methane combustion with the goal of understanding these effects, explaining contrasting reports, and learning how to improve the activity of supported Pd catalysts for this reaction in the low-temperature regime. This study relies on the synthesis of size-controlled Pd nanocrystals from 2 to 9 nm deposited onto high-surface area supports with similar textural properties but different surface chemistries: Al_2O_3, MgO, SiO_2, and $Ce_{0.8}Zr_{0.2}O_2$ (CZ80). Kinetic measurements reveal that the activity of palladium is only mildly sensitive to the nanocrystal size on all four supports, and that there is a strong trend with respect to support chemistry: acidic (Al_2O_3), inert (SiO_2) and reducible (CZ80) supports have activities over an order of magnitude larger compared to that of basic support MgO, but surprisingly alumina and ceria-zirconia deliver similar rates despite the known oxygen-donating capabilities of this latter support. Further kinetic and rate order measurements in the presence of steam demonstrate that these trends do not change and that the rate limiting step of methane combustion occurs on PdO.

2. EXPERIMENTAL SECTION

2.1. Synthesis of Pd nanocrystals (NCs). Palladium NCs syntheses were performed following previously reported procedures[43,51,52] with small modifications; in particular, solvents mixtures were used in place of pure 1-octadecene (ODE) to achieve reflux conditions that are known to improve size uniformity,[53] and different surfactant-to-palladium ratios were used to tune particle size control and uniformity. Briefly, palladium (II) acetylacetonate ($Pd(acac)_2$), solvents (1-dodecene (DDE), 1-tetradecene (TDE), or ODE), 1-oleylamine (OLAM) and in certain cases oleic acid (OLAC) are mixed in a three-neck flask (see table S1 for further details) and evacuated at RT for 15 min under stirring. Trioctylphosphine (TOP) was then added under evacuation and the mixture was heated to 50 °C for 30 minutes to remove all water and other impurities. At this point, the reaction mixture was a transparent yellow-orange colored solution. The reaction flask was then flushed with nitrogen and rapidly heated (~ 40°C min^{-1}) to the desired temperature. After 15 min of reaction at the appropriate temperature (see Table S1 for details) and under magnetic stirring, the solution was quickly cooled to RT by blowing compressed air on the outside of the flask and adding a water bath when the temperature was below 170°C. The particles were precipitated with isopropanol and ethanol, and separated by centrifugation (8000 RPM, 3 min) three times, with redissolution in a hexanes/OLAM solution (20 mL Hexanes: 100 µL OLAM) after each centrifugation step. Finally, the particles were dissolved in hexanes producing a deep black solution

2.2. Support Preparation. Alumina (Al_2O_3), silica (SiO_2), ceria-zirconia ($Ce_{0.8}Zr_{0.2}O_2$, or CZ80), and magnesia (MgO) were synthesized and calcined to obtain similar surface areas (ca. 100 m^2 g^{-1}) pore size (ca. 10 nm), and pore size distributions (centered at ~10 nm). Alumina was prepared by calcining Pluralox TH100/150 at 900 °C for 24 h using heating and cooling ramps of 3 °C min^{-1} in static air. Silica was prepared by calcining silica gel at 900 °C for 8 h using heating and cooling ramps of 3 °C min^{-1} in static air. Ceria-Zirconia was synthesized by inverse co-precipitation of cerium nitrate hexahydrate ($Ce(NO_3)_3 \cdot 6H_2O$) and zirconium (IV) oxynitrate hydrate ($ZrO(NO_3)_2 \cdot xH_2O$) using a previously published procedure[54] and then calcined at 700 °C for 5 h using heating and cooling ramps of 3 °C min^{-1} in static air. Magnesia was prepared following a previously published procedure[55] by calcining basic magnesium carbonate at 600 °C for 2 h using heating and cooling ramps of 10 °C min^{-1}. All supports were sieved below 180 µm grain size after calcination.

2.3. Catalyst Preparation. An appropriate amount of metal nanoparticles to give a nominal final loading of 0.5 wt. % Pd, ICP-OES was used to ensure actual weight loadings, (see Table S2 for details) was added to a dispersion of the support (Al_2O_3, MgO, SiO_2, or CZ80) in hexanes under vigorous stirring. In a typical procedure, 3 g of support were dispersed by sonication in 30 mL of hexanes and added with 1.6 mL of a 9.2 mg mL^{-1} solution of Pd NCs in hexanes. The mixture was left stirring for 15 min. The solid was recovered by centrifugation (8000 RPM, 3 min) and washed once with hexanes (30 mL), with sonication and centrifugation. The supernatant was discarded and the final powders were dried at 80 °C overnight and sieved below 180 µm grain size. Ligands were removed from the deposited Pd nanoparticles using a previously published rapid thermal annealing technique,[56] in which catalyst powders were carefully placed in a pre-heated 700°C furnace for 30 s (**ATTENTION: the high temperature in the furnace can cause severe burns and the insertion and removal of samples should be performed carefully and with heat-resistant gloves and with tongs**). All powders were sieved below 180 µm grain size after thermal annealing.

2.4. Characterization Techniques. N_2 physisorption and CO Chemisorption experiments were carried out on a Micromeritics 3Flex. For physisorption measurements, support powders were degassed in vacuum at 350 °C for 12 h prior to N_2 adsorption at liquid nitrogen temperature. For CO chemisorption, catalyst powders were placed in a U-shaped quartz reactor and then pretreated and degassed in the following manner: evacuated at 110 °C for 30 min, heated in flowing 5% O_2 in Ar at 300 °C for 30 min, evacuated at 300 °C for 30 min, reduced in flowing 5% H_2 in Ar at 300 °C for 1 h, and then evacuated at 300 °C for 4 h. CO adsorption experiments were conducted at 35 °C in the pressure range from 100 to 450 torr for Al_2O_3, SiO_2, and MgO-based systems and at -70 °C in an ethanol-dry ice bath in the pressure range from 2 to 20 torr for CZ80-based systems using a double isotherm to remove the contribution from physisorption.[57] Adsorption values were obtained by linear extrapolation to zero pressure.

Transmission electron microscopy (TEM) images were recorded on a FEI Tecnai transmission electron microscope equipped with an Orius CCD and a FEI Titan environmental transmission electron microscope equipped with a spherical aberration corrector in the image forming lens and a Gatan OneView camera operating at 200kV. Nanoparticle samples were dropcast onto TEM grids from their native hexanes solutions onto ultrathin carbon films supported on Cu TEM mesh grids. Supported catalyst TEM grids were prepared by dry deposition by lightly shaking a lacey carbon Cu-mesh TEM grid with catalyst powder in a plastic tube.

Small Angle X-ray Scattering (SAXS) measurements were performed at Beamline 1-5 at Stanford Synchrotron Radiation Lightsource (SSRL) of SLAC National Accelerator Laboratory using a Rayonix 165 SX CCD area detector. Scattering patterns were analyzed by fitting to a quantitative model using the IRENA package (available at usaxs.xray.aps.anl.gov/staff/ilavsky/irena.html from the APS) (Ilavsky, J. & Jemian, P. R. Irena: Tool suite for modeling and analysis of small-angle scattering)[58] to determine the size and size distribution of disperse nanocrystals of the as synthesized particles.

Quantitative elemental analysis of supported Pd catalysts were analyzed by an ICP-OES (Thermo Scientific ICAP 6300 Duo View Spectrometer). Catalyst powders were digested with a mixture of nitric acid (710 µL) and hydrochloric acid (660 µL) for seven hours, filtered, and then diluted before measurements.

2.5. Catalytic Measurements. All catalytic measurements were conducted at atmospheric pressure in a U-shaped quartz microreactor with an internal diameter of 1 cm. Catalyst (~20 mg) and bare alumina powders in a 1:10

dilution ratio were physically mixed and loaded into the reactor between two layers of granular acid-washed quartz resulting in a bed length of ca. 1 cm. The reactor was heated by a Micromeritics Eurotherm 2416 furnace while the temperature of the catalyst was measured with a K-type thermocouple inserted inside the reactor and touching the catalyst bed. No appreciable conversions were found when only quartz or bare supports were placed in the reactor in the range of temperatures used for this study.

Reaction mixtures (0.75-6% CH_4, 0.25-4% O_2, 0-12% H_2O, balance Ar) were prepared by passing a mixture of 5% or 20% CH_4 (certified standards, Airgas), 5% O_2 in Ar (certified standard, Airgas), and Ar (99.999%, Airgas) controlled by electronic thermal mass flow controllers (Brooks SLA5850) through a saturator filled with MilliQ water and maintained at the appropriate temperature with a J-KEM 210-K PID controller and K-type thermocouple in contact with the outside of the saturator. The saturator was bypassed for measurements without steam. Gas hourly space velocities (GSHV) were between 75,000-750,000 mL g^{-1} h^{-1}. An on-line gas chromatograph (GC) (Buck Scientific model 910), equipped with a thermal conductivity detector (TCD) and flame ionization detector (FIG) with a methanizer, and using Ar as the carrier gas was used to monitor the reactant and product streams.

Prior to measuring catalyst performance, each catalyst was cleaned under a flow of O_2 (5%) in Ar at 45 mL min^{-1} for 30 min at 300 °C. Then, the sample was cooled to initial measurement temperature under Ar flow and the reaction mixture was then introduced. Kinetic rates were measured at steady-state as determined by a stable CO_2 production signal. For kinetic rates, conversions of the limiting reactant were always kept below 2% conversion to guarantee differential working conditions. Turnover frequencies (TOF) were calculated on the basis of accessible metal surface area calculated from CO chemisorption measurements using the following equation:

$$\mathrm{TOF} = \frac{P M_{\mathrm{Pd}} \dot{V}_{\mathrm{CH_4}}}{R T m_{\mathrm{cat}} f_{\mathrm{cat}} D} \chi_{\mathrm{CH_4}} \qquad (1)$$

where P is the pressure of the reaction, M_{Pd} is the molar mass of Pd, $\dot{V}_{\mathrm{CH_4}}$ is the volumetric flow rate of CH_4, R is the universal gas constant, T is temperature, m_{cat} is the mass of the catalyst in the bed, f_{Pd} is the weight fraction of Pd in the catalyst, D is the dispersion of the catalysts as measured by CO chemisorption, and $\chi_{\mathrm{CH_4}}$ is the conversion of methane. Serial dilution experiments were performed to ensure no thermal nor mass transport limitations were present.

2.6. *in-situ* XAS Experiments. Pd K-edge (24350 eV) XAS data were collected at BL 4-1 at Stanford Synchrotron Radiation Lightsource (SSRL) using a Si (220) monochromator detuned by 50% and Lytle Detector. Athena software was used for data normalization.[59] Typically, 3 to 4 scans were averaged and a linear pre-edge was subtracted. Normalization was performed by unit edge jump. k-weighted EXAFS data in R-space were obtained by subtracting a polynomial background function to the normalized data and processing the resulting χ(k) signal through Fourier transform. Data were fitted in R-space using the Artemis software. Single scattering paths amplitude and phase shift were calculated using structural parameters from PdO and Pd crystal structure. A Be tube (OD 5mm, ID 3.8mm, L 65 mm; PF-60 grade Materion) was used as in-situ cell and an aluminum block was employed as heating element. Typically, 50 mg of catalyst (Pd 0.5 wt%, <80 mesh) were loaded into the reactor between quartz wool. After inserting reactor into the flow system, XAS spectra of the as-prepared catalyst was collected. The catalyst was then pretreated under a 45 mL min^{-1} flow of 5% O_2 in He at 300 °C for 30 min and then cooled to 220 °C under He. XAS spectra were again collected for the after-pretreatment state of the catalyst. The catalyst was then put under reaction flow conditions in the absence of water (1% CH_4 and 4% O_2 in He at 80 mL min^{-1}), while XAS spectra were continually recorded. Once the XAS scans were stable, water was introduced into the feed stream by flow the reaction gas through a saturator maintained at 20 °C (0.75% CH_4, 3% O_2, and 2.3% H_2O in He at 80 mL min^{-1}). Again, XAS spectra were recorded during this time until stable scans were observed.

2.7. DFT Calculations. All calculations were performed with The QUANTUM ESPRESSO code[60] using plane-wave DFT employing Vanderbilt ultrasoft pseudopotentials.[61] The BEEF-vdW exchange correlation functional[62] was used in all calculations. A 4x4x1 Monkhorst-Pack k-point sampling to model the Brillouin zone and a periodic unit cell containing 4 atomic layers were used, where the top two layers, together with the adsorbates, were allowed to relax whereas the bottom two layers were fixed in their bulk positions. The unit cell sizes were (2x2) for Pd(100) and PdO(101), and (3x3) for Pd(111) with 14 Å of vacuum between successive slabs. The plane-wave and density cutoff were 500 eV and 5,000 eV, respectively. Geometry optimizations were performed with a quasi-Newton algorithm as implemented in the Atomic Simulation Environment (ASE).[63] The convergence criterion for all structural optimizations was a maximum force of 0.05 eV/Å per atom. Transition states were determined using the climbing image-nudged elastic band (CI-NEB) approach.[64]

A self-consistent mean-field microkinetic model was solved using CatMap,[65] where rates were determined by solving the coupled differential equations numerically using the steady state approximation. Free energies were calculated combining the contributions from DFT calculations, ZPE, and entropy. For gas species, the entropy contribution was calculated using Shomate equations.[66] Contributions for adsorbed and transition state species due to vibrational entropy were calculated using the harmonic approximation. Further details of the microkinetic model can be found in the supplementary information.

3. RESULTS AND DISCUSSION

3.1. Synthesis of Well-Defined Pd-based Catalysts.

Uniform palladium nanocrystals (NCs) were synthesized via a modified synthesis[43,51,52] and deposited onto several supports (Al_2O_3, MgO, SiO_2, and $Ce_{0.8}Zr_{0.2}O_2$ (CZ80)) with similar textural properties (surface area, pore size distributions) to systematically study the structure-property relationships for Pd-catalyzed methane combustion. For this study, the particular range of sizes (2 to 9 nm) was selected because of the large change in the fraction of different sites (corners edges facets, etc.) that occurs in this size regime.[43–45,67] For simplicity, particles of 2.5, 3.7, 4.3, 6, and 8.2 nm average diameter will be labeled as x-small, small, medium, large, and x-large through the text. These uniform Pd NCs were prepared via thermal decomposition of Pd (II) acetylacetonate in mixtures of high boiling point solvents (octadecene (ODE), tetradecene (TDE), and/or dodecene (DDE)) in the presence of 1-oleylamine (OLAM), trioctylphosphine (TOP), and, in some samples, oleic acid (OLAC) (see Table S1 for synthesis details) to control size and uniformity and provide colloidal stability. Representative transmission electron microscopy (TEM) images, particle size analysis, small angle X-ray scattering (SAXS) measurements demonstrate qualitatively and quantitatively the high degree of uniformity of the as-synthesized Pd NCs and the level of control over size achieved by varying the surfactant-to-Pd precursor ratio (Figure 1, and Tables S1 and S4). The as-synthesized NCs are then deposited onto high surface area supports by adsorption from solution and activated via a fast thermal treatment to remove the ligands that would hinder reactivity.[56] As shown in Figure 2 and S1, and Tables S2 and S4, TEM analysis and CO chemisorption measurements confirm that the high degree of uniformity of all sizes of Pd NCs on all supports is maintained through deposition, ligand removal, and after rate measurements. Inspection of the x-large particles on SiO_2 reveals that the particles sintered during chemisorption measurements due to their poor dispersion (see Figure S2).

Control over the support textural properties was also achieved in order to reduce the number of variables affecting the final catalytic activity. In this study, the chosen supports were calcined such that their surface area, pore size, and pore volume were similar (see figure S3). The supports investigated in this study span relatively inert (SiO_2) to acidic (Al_2O_3) to basic (MgO) to active, oxygen-donating supports (CZ80). This element allowed us to better understand the effect of surface chemistries on the activity of Pd for methane combustion. Comparisons of the catalytic activity on the different supports allowed us to understand the effects of acidity and oxygen storage potential on reaction rates and mechanisms.

Overall, the structural characterization of the samples confirmed that the library of materials prepared in this work allowed us to unequivocally correlate structural features of the particles (fraction of specific sites at varying particle size), support chemistry, and reaction conditions to changes in catalytic activity because we are only varying one of these parameters at a time.

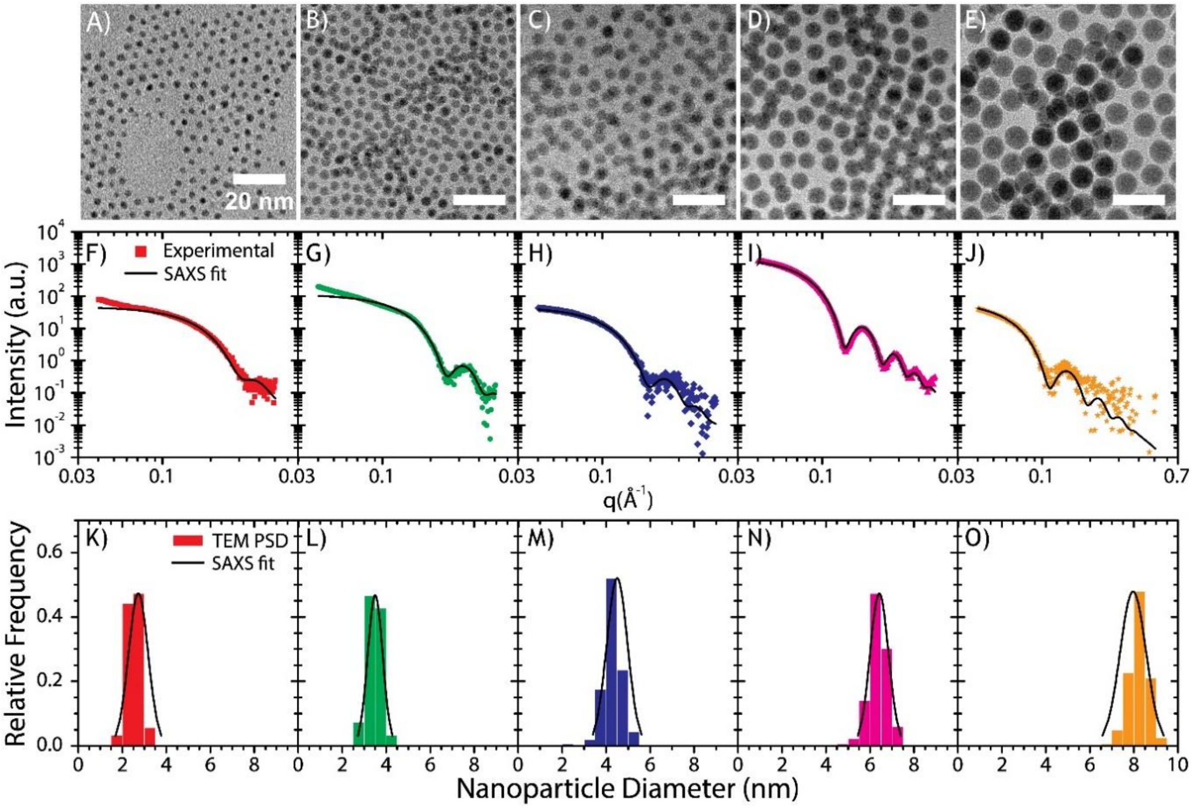

Figure 1. Representative TEM images (A-E), small angle X-ray scattering patterns (F-J), and particle size distributions (K-O) for uniform Pd NCS (from left to right x-small, small, medium, large, and x-large, respectively). For TEM measurements, N ≥ 300 counts.

3.2. Catalytic Methane Combustion.

3.2.1. Size Effects. Kinetic rate measurements were performed under lean conditions (O_2:CH_4 ratio of 4:1) initially in the absence of excess steam to replicate numerous studies reported in the literature. To ensure neither mass transport nor thermal diffusion limitations affected the results, very low conversions (<2%), high space velocities, and catalyst dilutions were used in each experiment. Tests were performed to confirm that dilution was sufficient to avoid temperature and concentration gradients for the reactor used in our studies (see figure S4).

Additionally, kinetic measurements were performed under true steady-state conditions (see figure S5), when rates were stable at each temperature step. Because of the peculiar PdO-Pd interconversion and restructuring occurring in Pd catalysts depending on reaction conditions, steady state measurements would sometimes need to wait long stabilization times (hours) before kinetic data could be taken. This phenomenon is likely not related to particle sintering or drastic shape effects given the characterization data of the particles after catalysis (see Figure 2 and Table S4). Turnover frequencies (TOFs) were calculated from rate measurements by measuring exposed Pd surface area via CO chemisorption on all the samples. Due to the various conditions used for measuring methane combustion turnover rates in the literature, comparisons are often difficult. Using previously reported rate orders[13,15] and assuming no water inhibition, the TOFs in our work, $4\text{x}10^{-4}$ to $3\text{x}10^{-2}$ s^{-1} at 220 °C, are comparable to those seen previously in literature for Pd-based catalysts[13,14,24,28,68,69] (see table S5). Normalized rate measurements revealed a weak size dependence for Pd-catalyzed combustion for all four support series (Al_2O_3, SiO_2, MgO, and CZ80), in which the difference in activity for different sizes is between 2 to 5 times (Figure 3 and S6, and table S5). The difference was larger than the error in rate measurement or particle size estimation (see figure S7).

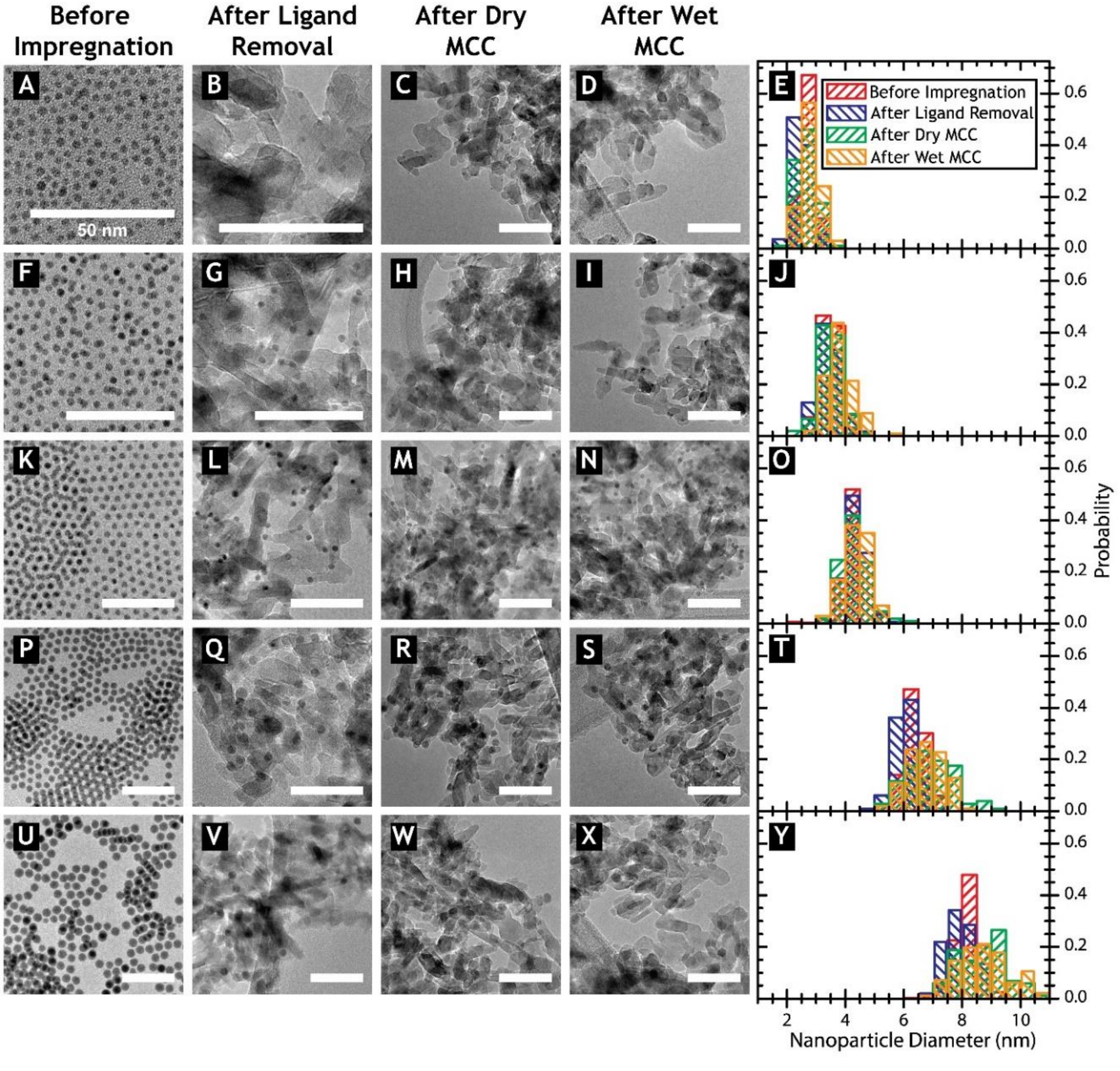

Figure 2. Representative TEM images of Pd NCs before impregnation, after ligand removal, after dry methane combustion, and after methane combustion in the presence of steam, and particle size distribution histograms (N ≥ 100 counts) for X-Small (A-E), Small (F-J), Medium (K-O), Large (P-T), X-Large (U-Y) Pd NCs on Al_2O_3, respectively.

Interestingly, it was not the smallest particles that deliver the highest rates; instead, particles of intermediate particle size around 4 to 5 nm showed the largest rates above all the supports tested. Despite the slight differences in turnover rates between Pd catalysts on different supports, the apparent activation energy had similar values of about 80 to 100 kJ mol^{-1} across all sizes and supports, suggesting that the rate limiting step for the reaction in all these catalysts was similar, likely the C-H activation on the Pd/PdO surface in accordance to other reports.[13,21]

We propose that the following are possible reasons for the observed mild structure sensitivity: oxidation state of the Pd phase,[21,70] strain effects on the Pd active phase,[71–73] proportion of different sites,[43–45,67] the relative proportion of PdO (101) to PdO (100) facets,[29,74] and chemisorption effects.[15,24]

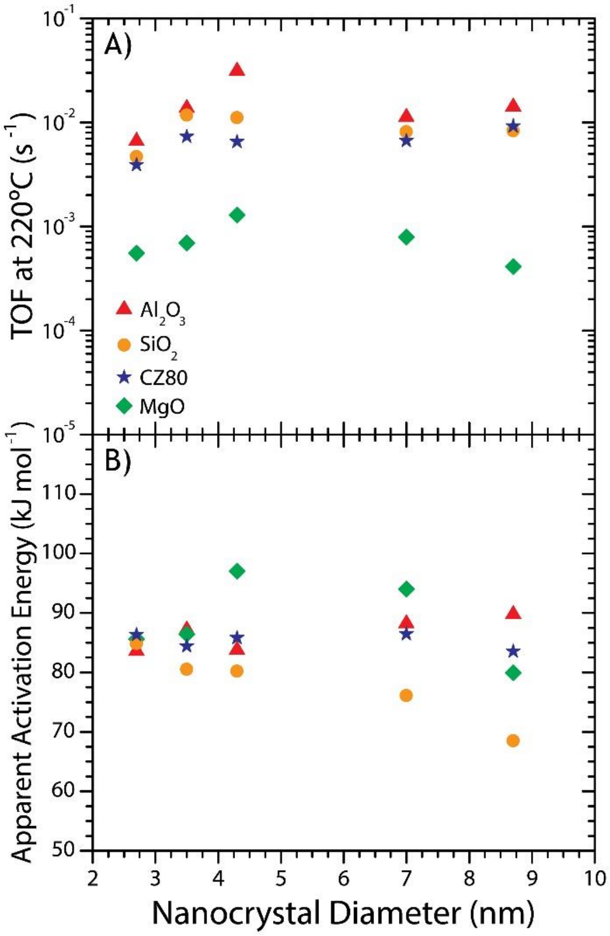

Figure 3. Turn-over Frequency (TOF) at 220 °C (A) and Apparent Activation Energy (B) for all support Pd NC samples as a function of size as calculated from Arrhenius fits. Rates were measured under the following conditions: 1% CH_4, 4% O_2 in Ar at 175,000 mL g_{cat}^{-1} h^{-1}.

In-situ X-ray absorption spectroscopy (XAS), DFT calculations, rate order experiments, a surface site model,[68] and post-catalysis characterization were implemented to understand which of these effects are likely contributing to the mild structure sensitivity. The oxidation state is extremely important for Pd-catalyzed methane combustion, controlling both the mechanism and reactivity of the Pd-based catalyst, in which the PdO phase is significantly more active than the Pd phase.[21,74] *In-situ* XAS measurements revealed that the palladium phase was PdO for three sizes tested (x-small, medium and large) of alumina supported Pd NCs, as evidenced qualitatively by XAS spectra in the X-ray absorption near-edge structure (XANES, Figure S8) and extended X-ray absorption fine structure (EXAFS, Figure 4) regions, and quantitatively by fits to the EXAFS spectra (see Figure 4 and Table S6). DFT calculations of the equilibrium state further corroborate that PdO is the thermodynamically stable phase under the working conditions used in these experiments (Figure S9). This data suggests that the oxidation state did not change with particle size and thus is not the cause for the observed structure sensitivity.

Strain effects have been shown to enhance catalytic rates, such as in propene metathesis[71] and oxygen reduction[72,73] reactions, by adjusting the bonding strength of reaction intermediates. As shown in Table S6, fits of EXAFS spectra demonstrated the bond lengths for the Pd-O, second shell Pd-Pd, and third shell Pd-Pd did not change with particle size for alumina supported catalysts, suggesting that strain effects are not the cause for the structure sensitivity.

Rate order experiments for O_2 and H_2O, which are in agreement with previous reports, [13,14,24] revealed that the apparent rate orders do not change with particle size (see figure S10 and table S7), suggesting that the reaction mechanism is not affected by particle size to a great extent. The combination of this information and the knowledge that the oxidation state of Pd (II) remains unchanged under reaction conditions suggests that the structure sensitivity may be caused by a small difference in the proportion of sites[43–45,67] or facets,[29,74] or by different relative proportion of exposed PdO (101) and (100) facets. To assess the effect of different proportions of sites, a previously developed physical model for cubo-octahedral NCs[67] was implemented. Fitting the model to scaling relationships (see Figure S11) demonstrates that in the size range of interest (2 to 9 nm) the fraction of surface sites from facets (coordination number (CN) > 8) is proportional to the diameter as $\sim d^{0.3}$, that of edge sites (CN = 7) to $\sim d^{-0.8}$, and that of corner sites (CN = 6) to $\sim d^{-2.1}$. While this model assumes the use of a metallic particle with an FCC crystal structure, whereas our materials are oxidized palladium during catalysis, we believe that this model is robust as the scaling relations do not drastically change with geometries and thus can be used to assess the proportion of different sites as the cause for the observed mild structure sensitivity.[43–45,67] Plotting the TOF for the different series of supported Pd catalysts revealed that the physical model does not fit the TOF's for all supports (R^2 < 0.6; Figure S11 and Table S8). This observation suggests that the structure sensitivity is not the only cause for the observed activity trend. It has to be highlighted that to calculate the TOF for these catalysts, CO chemisorption experiments were performed on the reduced catalysts. As discussed previously, differences on the order of 2-4 times have been attributed to the increase in

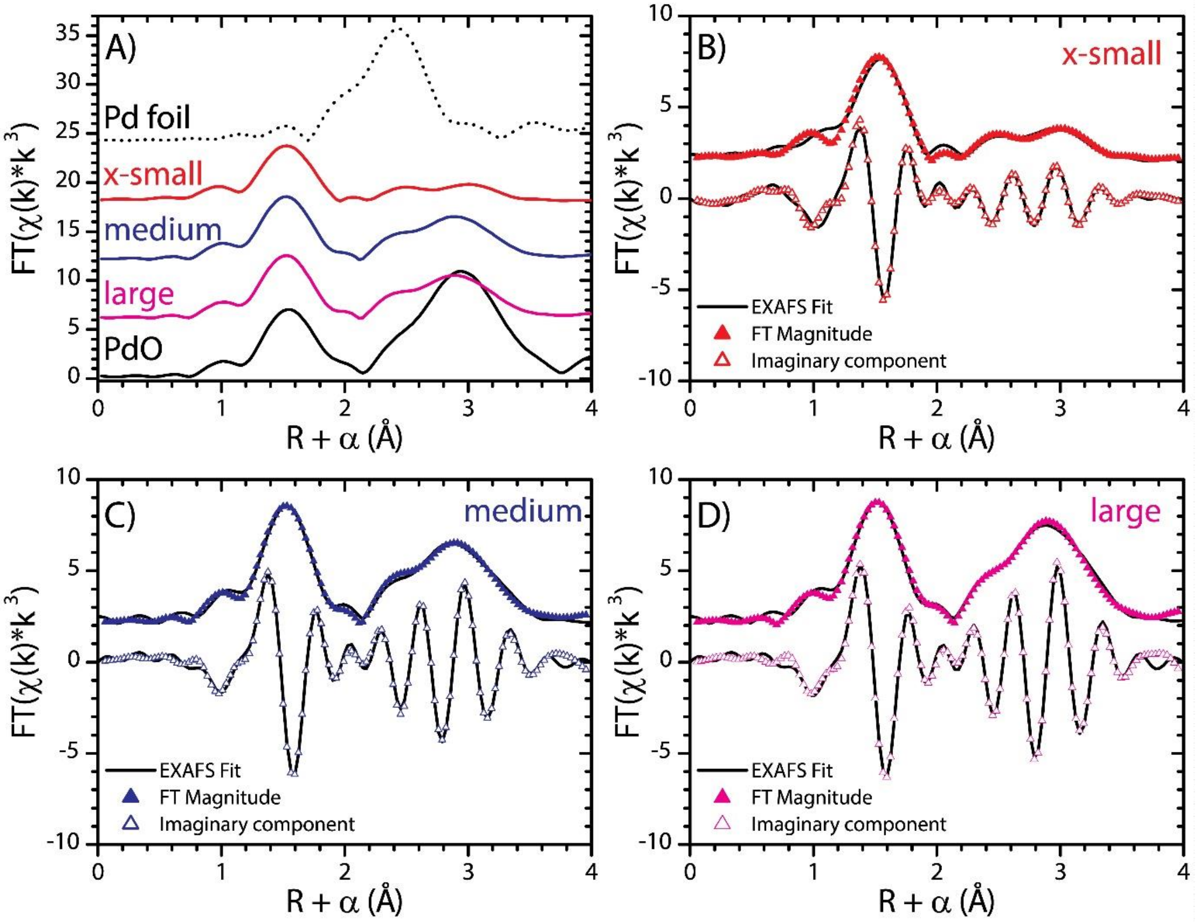

Figure 4. Comparison of EXAFS Fourier Transform (FT) magnitudes (A) in k^3-weighted, nonphase-corrected R-space for Al_2O_3 supported x-small, medium, and large nanocrystal samples under working conditions (1% CH_4 and 4% O_2 in Ar at 220 °C) and Pd and PdO standards. Curve-fits of EXAFS data for x-small Pd/Al_2O_3 (B), medium Pd/Al_2O_3 (C), and large Pd/Al_2O_3 (D) under working conditions (1% CH_4 and 4% O_2 in Ar at 220 °C) is shown for both the FT magnitude and imaginary components, with curve-fit parameters in Table S5.

surface area during oxidation of metallic Pd.[14,15,24] We believe that the fact that the size of the supported PdO nanocrystals is maintained after catalysis (both in the absence and presence of steam) (see Figure 2 and Table S4) suggest that the chemisorption results in this work are an accurate representation of the exposed surface area of the active phases. Thus, the observed mild structure sensitivity is not only caused by inconsistencies caused by performing CO chemisorption on the reduced catalysts.

Finally, a difference in proportion of exposed PdO(101) and (100) facets can also contribute to the differences in activity between samples. These two facets, which are the most thermodynamically stable,[75,76] are indeed known to have different performance.[29,30,74] In particular, it has been theoretically shown that the PdO(100) facet is more stable but less active than the PdO(101) facet.[77] In our case, it is rather difficult to obtain information about exposed facets during reaction conditions. Attempts to use HR-TEM to characterize the post-catalysis samples resulted in beam-induced artifacts that did not allow us to gain any trustable conclusion from this characterization. However, we cannot exclude that particles of different sizes and morphology may show preference for one exposed facet compared to another.

In conclusion, for these supported catalysts used in this study, the data showed that PdO is the most active phase under lean-burn conditions and that there is a mild sensitivity of the reaction to the particle size possibly due to the proportion of relatively extended PdO facets with a preferential crystallographic structure. This observation is in agreement with previous literature reports for supported Pd catalyst systems.[29,30,74] We believe that these results also suggest that previous contrasting reports of structure-sensitivity in Pd methane combustion may have also been a result of a combination of factors including varying proportions of sites and facets.

3.2.2. Support Effects. Comparison of the kinetic rate measurements for Pd deposited onto different supports showed that Al_2O_3, SiO_2, and CZ80 gave very similar performance at a given particle size, whereas MgO support drastically reduced the catalytic rates of supported Pd, but there were no substantial differences in the activation energies in the absence of water in the feed (see Figures 3 and S6). As shown from catalytic rates in Figures 3 and S6, a reducible support such as CZ80 appeared to not significantly affect intrinsic rates of the Pd phase. However, the significantly lower activity of MgO-supported catalyst suggests that acidity may have a strong effect on intrinsic activity.

Catalytic rates reported in Figures 3 and S6 demonstrated that the reaction mechanism is similar for each system and that CZ80 did not enhance Pd-catalyzed methane combustion activity. In order to test whether the ceria-zirconia support used in this study was reducible and could participate in oxidation reactions, we performed CO oxidation tests on Pd/CZ80 and Pd/Al_2O_3 catalysts prepared from the same Pd NC precursor. As previously shown,[43] CZ80-supported palladium catalysts showed significantly higher rates (>10 times, Figure S12) compared to alumina-supported Pd catalysts under CO oxidation conditions, thus demonstrating that the CZ80 used in this work could participate in the catalytic cycle with its reactive surface oxygens. The surprising fact that CZ80 did not increase Pd methane combustion rates suggests that activation of oxygen is not a limiting step under the conditions used in this study (excess oxygen). Further corroboration to the hypothesis that CZ80 did not directly affect rates came from rate order experiments which were also similar between Al_2O_3-supported catalysts and CZ80-supported catalysts (see Table S7). In comparison, reaction rate orders are rather different in CO oxidation for ceria- and alumina-supported Pd.[78]

With respect to support acid/base properties, MgO-supported catalysts showed significantly lower activities compared to the other three supports (Al_2O_3, SiO_2, and CZ80) (see Figures 3 and S6). Despite this lower activity, the activation energies were similar, suggesting that the active site or phase is likely to be similar for all four supports. There are two potential explanations for the lower rates observed on Pd/MgO catalysts that are related to either the electronic state of the PdO phase, or to strong adsorption of CO_2 on the catalytic surface. It has been suggested previously that MgO may stabilize an electron-rich PdO phase where the oxide anion is strongly basic.[31,79] This situation would lead to an increased stability of the PdO phase, and an increased oxygen vacancy formation energy. Since efficient C-H activation on PdO follows a Mars-van Krevelen mechanism with the oxide ion abstracting a proton and being further converted to water and desorbed,[13] the formation of oxygen vacancies plays a crucial part in the mechanism. Stabilization of the oxide ion by MgO support therefore leads to a decrease in rate. A second possibility is the formation of a magnesium carbonate phase in close contact with the palladium particles. MgO is known to adsorb CO_2 to form transient magnesium carbonate species.[80,81] These species may affect the surface of supported Pd particles, or the metal-support interface, thus blocking the active sites. Both hypotheses are consistent with the observed transient behavior of the catalysts on different supports. Despite there were no changes in the structure and oxidation state of the particles from *in-situ* XAS experiments when contacting the reaction mixture with the catalyst (figures S13 an S14), the transient methane conversion behavior for Pd/MgO showed large initial rates, likely due to a clean surface where a large fraction of oxide ions was available for the reaction, followed by a slow deactivation trend that lasted for hours, likely due to poisoning of the surface by either oxygen, formed water, or reaction intermediates (Figure S15). This behavior has been previously observed for pre-oxidized supported Pd particles and proposed to be caused by slight reduction of PdO.[13,31] However, while Al_2O_3-, SiO_2-, CZ80-supported Pd catalysts stabilize in 3 hours, the Pd/MgO samples typically took at least 12 hours before reaching steady-state conversions. This long deactivation period may have been caused by the slow adsorption of CO_2 and formation of magnesium carbonate, then responsible for decrease in activity of the supported Pd on basic supports such as MgO.

Overall, the catalytic characterization and *in*-situ XAS experiments demonstrate that the support chemistry and its interaction with the Pd does not strongly affect the intrinsic activity, nor the mechanism of supported Pd catalysts.

3.2.3. Water Effects. To understand the effect of water on Pd-catalyzed methane combustion, kinetic measurements were performed in the presence of excess steam for the Al_2O_3- and CZ80-supported samples. We focus on these two supports because they are the most promising in terms of catalytic rates, and because of the interesting comparison between alumina, a redox-inert support, and ceria-zirconia, which is instead considered as a support that participates in oxidation reactions. Similar to the experiments performed in the absence of steam, these kinetic measurements were performed under steady-state conditions when the catalysts provided stable rates (see figure S5B). As expected,[13,14,24] the rates were significantly lower in the presence of steam by over one order of magnitude, further demonstrating the severe deactivating effect of water on Pd catalysts for methane combustion. The apparent activation energies also significantly increased from 80-100 to 120-185 kJ mol^{-1} (see Figure 5 and S16 and Table S9). This increase in activation energy is expected because the measurements performed in dry conditions neglected water poisoning and its negative rate order. A similar weak size dependence to what was observed in the absence of steam was found for Pd/Al_2O_3 catalysts, with rates on intermediate Pd particles about 4-5 times those on smaller or larger sizes, whereas similar rates were observed for Pd/CZ80 materials (see Figure 5 and S16 and Table S9). Interestingly, the activation energies increased at increasing particle size for the Al_2O_3-supported Pd catalysts, while they did not change appreciably for the CZ80-support series. In literature, the reported activation energy varies from 135 to 185 kJ mol^{-1} when the water inhibition effect is accounted for.[13,14,24] Repeated kinetic rate measurements for the Pd/Al_2O_3 study demonstrated that the error in the values of the apparent activation energies in this study range between 1 and 15 kJ mol^{-1} (see figure S17), suggesting that the difference between activation energies is statistically significant. Despite these differences, the rate order for water across different Pd NC sizes and on both CZ80 and Al_2O_3 is -1 in agreement with literature studies (see Table S7).[13–16,24]

This discrepancy may be explained by different PdO particle morphologies on the two supports. The particles may have different proportions of sites on each support. In the case of alumina, the proportion of sites could change more drastically than the particles on CZ80 which would result in the increasing activation energy pattern on alumina. This element would also suggest that on ceria-zirconia, all sites are uniformly affected by water, whereas on alumina, the sites may be affected by water to different extents (hence the different activation energy), but that overall produce the same rates probably due to different intrinsic activities.

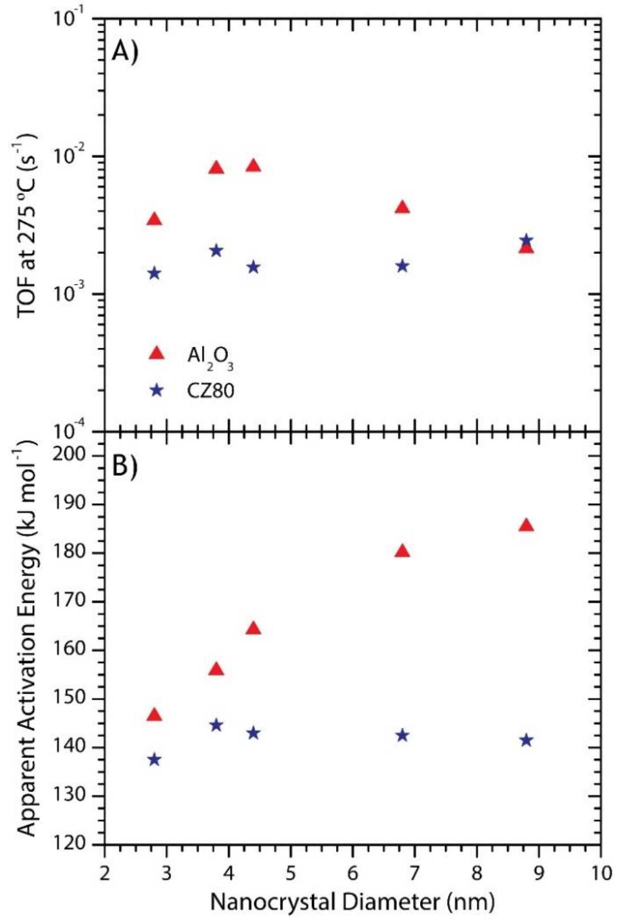

Figure 5. TOF at 275°C (A) and Apparent Activation Energy (B) for all support Pd NC samples as a function of size as calculated from Arrhenius fits. Rates were measured under the following conditions: 0.75% CH_4, 3% O_2, 4.2% H_2O in Ar at 75,000 mL g_{cat}^{-1} h^{-1}.

There are two hypotheses to explain the observed deactivation behavior: i) changes in Pd oxidation state or structure in the presence of water; ii) poisoning and competition for sites between water and oxygen. We first investigated how structural changes and variation in oxidation state may have affected the activity. *In-situ* XAS radial distributions demonstrated that the state and fine structure of the Pd particles was not significantly modified upon introduction of steam to the feed stream. This same effect was observed across different sizes of palladium NCs (x-small, medium, and large) supported on Al_2O_3 (figures S13 and S14). Previous work has suggested that the formation of surface hydroxyls and subsequent diffusion to sub-PdO layers leads to deactivation in the presence of steam.[49] Our *in-situ* XAS experiments do not support this argument for the deactivation because no major differences were observed in the bulk Pd structure once water was introduced in the reaction atmosphere. *Ex-situ* TEM characterization after catalytic reactions both in the absence and presence of steam demonstrated that the particles maintain their size after the kinetic studies (Figure 2 and table S4). This element further demonstrated that the reaction atmosphere did not significantly affect the structure, nor cause severe sintering under the conditions of our study. Thus, the observed poisoning effect and activation energy trends are likely not caused by the formation of $Pd(OH)_2$ in the bulk or other changes in the Pd oxidation state and/or structure.

Another possible explanation for water poisoning is the competitive adsorption of water on sites for both oxygen and methane activation, as presented in previous models and reports.[13,14,47] According to these models, water competes with methane for sites and due to the strong binding of water on PdO, the surface would likely be saturated with hydroxyl species leaving few sites for methane and oxygen activation, thus resulting in a significant decrease in combustion rates. Rate order studies were consistent with this mode of water poisoning. As discussed previously in literature, rate orders provide an idea of the coverage of species participating in catalytic reactions.[44,82] The strong negative rate order, -1, for water on multiple sizes of supported Pd NCs and on both Al_2O_3 and CZ80 (Table S7) implied that water is strongly bound to the PdO surface, and that water surface coverage is near unity. Differences in transient behavior between experiments in the absence and presence of steam are also consistent with this conclusion.

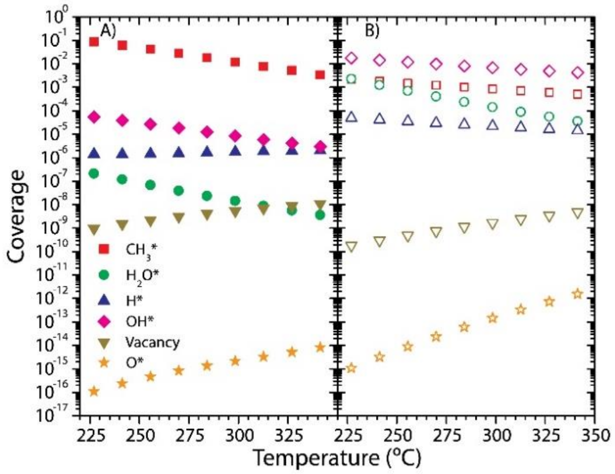

Figure 6. The coverage results from microkinetic model on PdO(101) under dry conditions (A) (1% CH_4, 4% O_2, and balance inert gas) and under wet conditions (B) (0.75% CH_4, 3% O_2, 4.2% H_2O, and balance inert gas).

As shown in Figure S18, the catalytic activity in the presence of steam stabilized typically within approximately 45 min, in comparison to at least 180 min needed in the absence of steam. In the presence of large concentrations of steam, the strong affinity of PdO for water causes rapid coverage of the surface with hydroxyls such that equilibrium is rapidly achieved, resulting in a significantly shorter time to reach steady state. However, in the absence of steam, the water produced by the reaction would slowly adsorb onto the PdO surface and longer times are needed to reach equilibrium, in accordance to other studies performed in the absence of water,[21,70] where long equilibrium times were required before collecting kinetic data. DFT calculations were used to produce a microkinetic model that further supported the water adsorption model proposed with the experimental data. Figure 6 shows the coverage results from the microkinetic model calculations (further details on the all the elementary steps in microkinetic model are shown in Table S3). In the presence of high levels of steam, there was a significant increase in occupation of adsorption sites by intermediate species (hydrogen and hydroxyls). This phenomenon led to a drop in the turnover frequency of methane combustion by an order of magnitude at 500 K (as shown in Figure S19).

4. CONCLUSIONS

In conclusion, we have developed a fundamental understanding of structure-property relationships for supported Pd catalysts through the use of uniform Pd NCs deposited on a variety of supports with similar textural properties but different surface chemistry. Through kinetic measurements, characterization experiments, and implementation of a model, we demonstrated that PdO is the most active phase for methane complete combustion and its activity is mildly structure-sensitive likely due to multiple factors such as proportion of sites and ratio of PdO(101) facets to PdO(100) facets. Comparison of activity of Pd NC deposited on different supports revealed a strong deactivation effect by basic supports (MgO) and that supports do not participate in the rate limiting step of Pd-catalyzed methane combustion in other supported nanoparticle systems. Further kinetic measurements, characterization experiments, and DFT-calculations demonstrated that water caused severe decrease in activity due to dissociation and high coverage levels on the PdO surface at high water chemical potentials and low temperatures. We believe this work settles the debated issues of structure sensitivity, support effects, and water inhibition for similar supported Pd methane complete combustion catalysts and acknowledge the difficulty of extending this understanding to more complicated Pd-based catalysts.[83–85] Overall, this study provides insights into the design features required for more active methane combustion catalysts.

ASSOCIATED CONTENT

Supporting Information. Additional experimental details on materials, microkinetic model, and phase diagrams; Additional TEM images and particles size distributions of supported catalysts; N_2 Physisorption Isotherm and Pore Size Distributions; Methane combustion Arrhenius Plots; Transient Methane Combustion Conversion Data; Additional XANES and EXAFS Spectra; Pd Phase Diagram; Rate Order Kinetic Measurement; Physical Model Analysis Plots; CO Oxidation Lightoff and Kinetic Measurements; Plot of Ratio of Methane Combustion Rates in the presence and absence based on Microkinetic Modeling; Tabulated details of NC synthetic parameters; Tabulated TEM and SAXS NC size data; Tabulated methane combustion kinetic data in presence and absence of water; and Tabulated CO chemisorption data; Tabulated Microkinetic Model Reactions; Tabulated EXAFS Fit Parameters; Tabulated Apparent Rate Orders; Tabulated Physical Model Fit Parameters. The Supporting information is available free of charge on ACS Publications website at DOI :

AUTHOR INFORMATION

Corresponding Author

*mcargnello@stanford.edu

Notes

The authors declare no competing financial interest.

ACKNOWLEDGMENT

We gratefully acknowledge support from the U.S. Department of Energy, Office of Sciences, Office of Basic Energy Sciences, to the SUNCAT Center for Interface Science and Catalysis. M.C. acknowledges support from the School of Engineering at Stanford University and from a Terman Faculty Fellowship. E. D. G. acknowledges support from the National Science Foundation Graduate Research Fellowship under Grant DGE-1656518. L. W. was supported by the US Department of Energy (DoE) under the Laboratory Directed Research and Development. Part of this work was performed at the Stanford Nano Shared Facilities (SNSF), supported by the National Science Foundation under award ECCS-1542152. Part of this work was performed at the Beamline 1-5 at Stanford Synchrotron Radiation Lightsource (SSRL) of SLAC National Accelerator Laboratory, and use of the SSRL is supported by the U.S. Department of Energy, Office of Science, Office of Basic Energy Sciences under Contract No. DE-AC02-76SF00515. We would like to thank Prof. Curtis W. Frank and Prof. Stacey Bent (Stanford University) for shared laboratory space. We also thank Dr. Ai Leen Koh for her support while performing TEM experiments.

REFERENCES

(1) Mallapragada, D. S.; Duan, G.; Agrawal, R. *Energy Policy* **2014**, *67*, 499–507.

(2) Lee, J. G.; Jeon, O. S.; Hwang, H. J.; Jang, J.; Lee, Y.; Hyun, S. H.; Shul, Y. G. *Electrochim. Acta* **2016**, *191*, 677–686.

(3) Qu, J.; Wang, W.; Chen, Y.; Deng, X.; Shao, Z. *Appl. Energy* **2016**, *164*, 563–571.

(4) Guo, X.; Fang, G.; Li, G.; Ma, H.; Fan, H.; Yu, L.; Ma, C.; Wu, X.; Deng, D.; Wei, M.; Tan, D.; Si, R.; Zhang, S.; Li, J.; Sun, L.; Tang, Z.; Pan, X.; Bao, X. *Science.* **2014**, *344*, 616–619.

(5) Horn, R.; Schlögl, R. *Catal. Letters* **2015**, *145*, 23–39.

(6) Camuzeaux, J. R.; Alvarez, R. A.; Brooks, S. A.; Browne, J. B.; Sterner, T. *Environ. Sci. Technol.* **2015**, *49*, 6402–6410.

(7) Overview of Greenhouse Gases https://www.epa.gov/ghgemissions/overview-greenhouse-gases, accessed October 6, 2017.

(8) Colussi, S.; Gayen, A.; Farnesi Camellone, M.; Boaro, M.; Llorca, J.; Fabris, S.; Trovarelli, A. *Angew. Chemie Int. Ed.* **2009**, *48*, 8481–8484.

(9) Shan, J.; Huang, W.; Nguyen, L.; Yu, Y.; Zhang, S.; Li, Y.; Frenkel, A. I.; Tao, F. F. *Langmuir* **2014**, *30*, 8558–8569.

(10) Shi, L.; Yang, G.; Tao, K.; Yoneyama, Y.; Tan, Y.; Tsubaki, N. *Acc. Chem. Res.* **2013**, *46*, 1838–1847.

(11) Tao, F. F.; Shan, J.; Nguyen, L.; Wang, Z.; Zhang, S.; Zhang, L.; Wu, Z.; Huang, W.; Zeng, S.; Hu, P. *Nat. Commun.* **2015**, *6*, 7798.

(12) Xiao, T.; Ji, S.; Wang, H.; Coleman, K. S.; Green, M. L. . *J. Mol. Catal. A Chem.* **2001**, *175*, 111–123.

(13) Fujimoto, K.; Ribeiro, F. H.; Avalos-borja, M.; Iglesia, E. *J. Catal.* **1998**, *179*, 431–442.

(14) Ribeiro, F. H.; Chow, M.; Dalla Betta, R. A. *Journal of Catalysis*. 1994, pp 537–544.

(15) Zhu, G.; Han, J.; Zemlyanov, D. Y.; Ribeiro, F. H. *J. Am. Chem. Soc.* **2004**, *126*, 9896–9897.

(16) Zhu, G.; Han, J.; Zemlyanov, D. Y.; Ribeiro, F. H. *J. Phys. Chem. B* **2005**, *109*, 2331–2337.

(17) Cook, A. K.; Schimler, S. D.; Matzger, A. J.; Sanford, M. S. *Science.* **2016**, *351*, 1421–1424.

(18) Smith, K. T.; Berritt, S.; Gonzalez-Moreiras, M.; Ahn, S.; Smith, M. R.; Baik, M.-H.; Mindiola, D. J. *Science.* **2016**, *351*, 1424–1427.

(19) Anderson, R. B.; Stein, K. C.; Feenan, J. J.; Hofer, L. J. E. *Ind. Eng. Chem.* **1961**, *53*, 809–812.

(20) Cullis, C. F.; Willatt, B. M. *J. Catal.* **1983**, *83*, 267–285.

(21) Chin, Y. H.; Buda, C.; Neurock, M.; Iglesia, E. *J. Am. Chem. Soc.* **2013**, *135*, 15425–15442.

(22) Lyubovsky, M.; Pfefferle, L. *Catal. Today* **1999**, *47*, 29–44.

(23) Farrauto, R. J.; Hobson, M. C.; Kennelly, T.; Waterman, E. M. *Appl. Catal. A Gen.* **1992**, *81*, 227–237.

(24) Monteiro, R. .; Zemlyanov, D.; Storey, J. .; Ribeiro, F. . *J. Catal.* **2001**, *199*, 291–301.

(25) Graham, G. W.; Poindexter, B. D.; Remillard, J. T.; Weber, W. H. *Top. Catal.* **1999**, *8*, 35–43.

(26) Boudart, M.; Djega-Mariadassou, G. *Kinetics of Heterogeneous Catalytic Reactions*; Princeton University Press, 1984.

(27) Baldwin, T. R.; Burch, R. *Appl. Catal.* **1990**, *66* (1), 337–358.

(28) Hicks, R. F.; Qi, H.; Young, M. L.; Lee, R. G. *J. Catal.* **1990**, *122*, 280–294.

(29) Martin, N. M.; Van den Bossche, M.; Hellman, A.; Grönbeck, H.; Hakanoglu, C.; Gustafson, J.; Blomberg, S.; Johansson, N.; Liu, Z.; Axnanda, S.; Weaver, J. F.; Lundgren, E. *ACS Catal.* **2014**, *4*, 3330–3334.

(30) Weaver, J. F.; Hakanoglu, C.; Hawkins, J. M.; Asthagiri, A. *J. Chem. Phys.* **2010**, *132*, 24709.

(31) Yoshida, H.; Nakajima, T.; Yazawa, Y.; Hattori, T. *Appl. Catal. B Environ.* **2007**, *71*, 70–79.

(32) Hoflund, G. B.; Li, Z.; Epling, W. S.; Göbel, T.; Schneider, P.; Hahn, H. *React. Kinet. Catal. Lett.* **2000**, *70*, 97–103.

(33) Farrauto, R. J.; Lampert, J. K.; Hobson, M. C.; Waterman, E. M. *Appl. Catal. B Environ.* **1995**, *6*, 263–270.

(34) Persson, K.; Ersson, A.; Jansson, K.; Iverlund, N.; Järås, S. *J. Catal.* **2005**, *231*, 139–150.

(35) Neyestanaki, A. K.; Kumar, N.; Lindfors, L.-E. *Appl. Catal. B Environ.* **1995**, *7*, 95–111.

(36) Okumura, K.; Matsumoto, S.; Nishiaki, N.; Niwa, M. *Appl. Catal. B Environ.* **2003**, *40*, 151–159.

(37) Colussi, S.; Trovarelli, A.; Groppi, G.; Llorca, J. *Catal. Commun.* **2007**, *8*, 1263–1266.

(38) Widjaja, H.; Sekizawa, K.; Eguchi, K. *Bull. Chem. Soc. Jpn.* **1999**, *72*, 313–320.

(39) Groppi, G.; Cristiani, C.; Lietti, L.; Ramella, C.; Valentini, M.; Forzatti, P. *Catal. Today* **1999**, *50*, 399–412.

(40) Ciuparu, D.; Altman, E.; Pfefferle, L. *J. Catal.* **2001**, *203*, 64–74.

(41) Ciuparu, D.; Bozon-Verduraz, F.; Pfefferle, L. *J. Phys. Chem. B* **2002**, *106*, 3434–3442.

(42) Schwartz, W. R.; Pfefferle, L. D. *J. Phys. Chem. C* **2012**, *116*, 8571–8578.

(43) Cargnello, M.; Doan-Nguyen, V. V. T.; Gordon, T. R.; Diaz, R. E.; Stach, E. a.; Gorte, R. J.; Fornasiero, P.; Murray, C. B. *Science.* **2013**, *341*, 771–773.

(44) Shekhar, M.; Wang, J.; Lee, W.-S.; Williams, W. D.; Kim, S. M.; Stach, E. A.; Miller, J. T.; Delgass, W. N.; Ribeiro, F. H. *J. Am. Chem. Soc.* **2012**, *134*, 4700–4708.

(45) Williams, W. D.; Shekhar, M.; Lee, W. S.; Kispersky, V.; Delgass, W. N.; Ribeiro, F. H.; Kim, S. M.; Stach, E. A.; Miller, J. T.; Allard, L. F. *J. Am. Chem. Soc.* **2010**, *132*, 14018–14020.

(46) Monai, M.; Montini, T.; Chen, C.; Fonda, E.; Gorte, R. J.; Fornasiero, P. *ChemCatChem* **2015**, *7*, 2038–2046.

(47) Gélin, P.; Urfels, L.; Primet, M.; Tena, E. *Catal. Today* **2003**, *83*, 45–57.

(48) Burch, R.; Urbano, F. J.; Loader, P. K. *Appl. Catal. A Gen.* **1995**, *123*, 173–184.

(49) Roth, D.; Gélin, P.; Primet, M.; Tena, E. *Appl. Catal. A Gen.* **2000**, *203*, 37–45.

(50) Schwartz, W. R.; Ciuparu, D.; Pfefferle, L. D. *J. Phys. Chem. C* **2012**, *116*, 8587–8593.

(51) Cargnello, M.; Doan-Nguyen, V. V. T.; Murray, C. B. *AIChE J.* **2016**, *62*, 392–398.

(52) Kim, S. W.; Park, J.; Jang, Y.; Chung, Y.; Hwang, S.; Hyeon, T.; Kim, Y. W. *Nano Lett.* **2003**, *3*, 1289–1291.

(53) Lynch, J.; Zhuang, J.; Wang, T.; LaMontagne, D.; Wu, H.; Cao, Y. C. *J. Am. Chem. Soc.* **2011**, *133*, 12664–12674.

(54) Cargnello, M.; Montini, T.; Polizzi, S.; Wieder, N. L.; Gorte, R. J.; Graziani, M.; Fornasiero, P. *Dalt. Trans.* **2010**, *39*, 2122–2127.

(55) Bartley, J. K.; Xu, C.; Lloyd, R.; Enache, D. I.; Knight, D. W.; Hutchings, G. J. *Appl. Catal. B Environ.* **2012**, *128*, 31–38.

(56) Cargnello, M.; Chen, C.; Diroll, B. T.; Doan-Nguyen, V. V. T.; Gorte, R. J.; Murray, C. B. *J. Am. Chem. Soc.* **2015**, *137*, 6906–6911.

(57) Tanabe, T.; Nagai, Y.; Hirabayashi, T.; Takagi, N.; Dohmae, K.; Takahashi, N.; Matsumoto, S.; Shinjoh, H.; Kondo, J. N.; Schouten, J. C.; Brongersma, H. H. *Appl. Catal. A Gen.* **2009**, *370*, 108–113.

(58) Ilavsky, J.; Jemian, P. R. *J. Appl. Crystallogr.* **2009**, *42*, 347–353.

(59) Ravel, B.; Newville, M. *J. Synchrotron Rad.* **2005**, *12*, 537–541.

(60) Giannozzi, P.; Baroni, S.; Bonini, N.; Calandra, M.; Car, R.; Cavazzoni, C.; Ceresoli, D.; Chiarotti, G. L.; Cococcioni, M.; Dabo, I.; Dal Corso, A.; de Gironcoli, S.; Fabris, S.; Fratesi, G.; Gebauer, R.; Gerstmann, U.; Gougoussis, C.; Kokalj, A.; Lazzeri, M.; Martin-Samos, L.; Marzari, N.; Mauri, F.; Mazzarello, R.; Paolini, S.; Pasquarello, A.; Paulatto, L.; Sbraccia, C.; Scandolo, S.; Sclauzero, G.; Seitsonen, A. P.; Smogunov, A.; Umari, P.; Wentzcovitch, R. M. *J. Phys. Condens. Matter* **2009**, *21* (39), 395502.

(61) Laasonen, K.; Car, R.; Lee, C.; Vanderbilt, D. *Phys. Rev. B* **1991**, *43*, 6796–6799.

(62) Wellendorff, J.; Lundgaard, K. T.; Møgelhøj, A.; Petzold, V.; Landis, D. D.; Nørskov, J. K.; Bligaard, T.; Jacobsen, K. W. *Phys. Rev. B* **2012**, *85*, 235149.

(63) Bahn, S. R.; Jacobsen, K. W. *Comput. Sci. Eng.* **2002**, *4*, 56–66.

(64) Henkelman, G.; Uberuaga, B. P.; Jónsson, H. *J. Chem. Phys.* **2000**, *113*, 9901–9904.

(65) Medford, A. J.; Shi, C.; Hoffmann, M. J.; Lausche, A. C.; Fitzgibbon, S. R.; Bligaard, T.; N?rskov, J. K. *Catal. Letters* **2015**, *145*, 794–807.

(66) Shomate, C. H. *J. Phys. Chem.* **1954**, *58*, 368–372.

(67) Van Hardeveld, R.; Hartog, F. *Surf. Sci.* **1969**, *15*, 189–230.

(68) Shen, J.; Hayes, R. E.; Wu, X.; Semagina, N. *ACS Catal.* **2015**, 5, 2916–2920.

(69) Roth, D.; Gélin, P.; Kaddouri, A.; Garbowski, E.; Primet, M.; Tena, E. *Catal. Today* **2006**, *112*, 134–138.

(70) Chin, Y.-H.; García-Diéguez, M.; Iglesia, E. *J. Phys. Chem. C* **2016**, *120*, 1446–1460.

(71) Amakawa, K.; Sun, L.; Guo, C.; Hävecker, M.; Kube, P.; Wachs, I. E.; Lwin, S.; Frenkel, A. I.; Patlolla, A.; Hermann, K.; Schlögl, R.; Trunschke, A. *Angew. Chemie Int. Ed.* **2013**, *52*, 13553–13557.

(72) Wang, H.; Xu, S.; Tsai, C.; Li, Y.; Liu, C.; Zhao, J.; Liu, Y.; Yuan, H.; Abild-Pedersen, F.; Prinz, F. B.; Nørskov, J. K.; Cui, Y. *Science.* **2016**, *354*, 1031–1036.

(73) Friebel, D.; Viswanathan, V.; Miller, D. J.; Anniyev, T.; Ogasawara, H.; Larsen, A. H.; O'Grady, C. P.; Nørskov, J. K.; Nilsson, A. *J. Am. Chem. Soc.* **2012**, *134*, 9664–9671.

(74) Hellman, A.; Resta, A.; Martin, N. M.; Gustafson, J.; Trinchero, A.; Carlsson, P.-A.; Balmes, O.; Felici, R.; van Rijn, R.; Frenken, J. W. M.; Andersen, J. N.; Lundgren, E.; Grönbeck, H. *J. Phys. Chem. Lett.* **2012**, *3*, 678–682.

(75) Weaver, J. F. *Chem. Rev.* **2013**, *113*, 4164–4215.

(76) Rogal, J.; Reuter, K.; Scheffler, M. *Phys. Rev. B* **2004**, *69*, 75421.

(77) Van den Bossche, M.; Grönbeck, H. *J. Am. Chem. Soc.* **2015**, *137*, 12035–12044.

(78) Bunluesin, T.; Putna, E. S.; Gorte, R. J. *Catal. Letters* **1996**, *41*, 1–5.

(79) Yazawa, Y.; Yoshida, H.; Hattori, T. *Appl. Catal. A Gen.* **2002**, *237*, 139–148.

(80) Lee, S. C.; Choi, B. Y.; Lee, T. J.; Ryu, C. K.; Ahn, Y. S.; Kim, J. C. *Catal. Today* **2006**, *111*, 385–390.

(81) Singha, R. K.; Yadav, A.; Agrawal, A.; Shukla, A.; Adak, S.; Sasaki, T.; Bal, R. *Appl. Catal. B Environ.* **2016**, *191*, 165–178.

(82) Borodzinski, A.; Bond, G. C. *Catal. Rev.* **2008**, *50*, 379–469.

(83) Senftle, T. P.; van Duin, A. C. T.; Janik, M. J. *ACS Catal.* **2015**, *5*, 6187–6199.

(84) Senftle, T. P.; van Duin, A. C. T.; Janik, M. J. *ACS Catal.* **2017**, *7*, 327–332.

(85) Cargnello, M.; Jaen, J. J. D.; Garrido, J. C. H.; Bakhmutsky, K.; Montini, T.; Gamez, J. J. C.; Gorte, R. J.; Fornasiero, P. *Science.* **2012**, *337*, 713–717.

Table of Contents (TOC) graphic.